Effect of Oxygen Adsorption on Electrical and Thermoelectrical Properties of Monolayer MoS_2

Swarup Deb,* Pritam Bhattacharyya, Poulab Chakrabarti, Himadri Chakraborti, Kantimay Das Gupta, Alok Shukla, and Subhabrata Dhar†
Department of Physics, Indian Institute of Technology Bombay, Powai, Mumbai 400076, India

(Received 7 March 2020; revised 4 June 2020; accepted 19 August 2020; published 11 September 2020)

The electrical and thermoelectrical properties of strictly monolayer MoS_2 films, grown using a microcavity-based CVD growth technique, are studied under diverse environmental and annealing conditions. The resistance of a monolayer MoS_2 device fabricated on an as-grown continuous single-layer film is found to be reduced by about six orders of magnitude upon annealing in vacuum at 525 K. The Seebeck coefficient of the layer is also reduced by almost an order of magnitude upon annealing. When the sample is exposed to an oxygen atmosphere, these parameters return to their previous values. It is found that the electron concentration, the mobility, and the thermoelectric power of the material can be varied significantly by annealing. Once a particular resistive state is established, it remains unchanged as long as the layer is not exposed to an oxygen environment. This may offer a unique way to control doping in the material provided an effective encapsulation method is devised. Such control is an important step forward for device applications. The effect is attributed to the passivation of disulfur-vacancy donors present in the MoS_2 film by physisorbed oxygen molecules. Band-structure calculations using density-functional theory are carried out, the results of which validate this picture.

DOI: 10.1103/PhysRevApplied.14.034030

I. INTRODUCTION

Two-dimensional (2D) materials, particularly transition-metal dichalcogenides (TMDs), such as MoS_2, $MoSe_2$, WS_2, etc., have emerged as materials for the next generation of logic, electronic, and optoelectronic devices and of energy-related technologies [1–4]. Mechanical exfoliation [5] and chemical vapor deposition (CVD) [6,7] are two of the most widely accepted techniques for preparing single-layer 2D samples. Both of these techniques have positive and negative sides. For example, exfoliated samples are superior in quality but fail in terms of scalability. The typical size of the monolayer regions in these flakes is not more than a few tens of micrometers [8,9]. Therefore, the fabrication of large-scale integrated circuits is not possible on such layers. On the other hand, CVD can provide monolayers with much larger area coverage [10–12]. However, these films often suffer from a high density of defects and grain boundaries [13,14]. Irrespective of the preparation technique, the increased surface-to-volume ratio makes these materials vulnerable to the ambient environment. It should be noted that chalcogen vacancies, which act as donors, are omnipresent in these materials [15,16]. In principle, these defects can influence the surface adsorption, which in turn can passivate these donors, affecting both the concentration and the mobility of the carriers in the layer. If the density of the adsorbates that passivate chalcogen-vacancy donors can be stabilized on the film surface by some means, one can tune the doping level of the material, an important step towards device applications. It should be mentioned that the optical properties of the film can also be affected by surface adsorption [17]. In fact, there have been recent studies of the effects of defect passivation on the optical properties of CVD-grown monolayer TMD films [18–21]. However, the influence of adsorption on the electronic properties of monolayer TMDs has hardly been studied so far.

Thermoelectrics have attracted a great deal of attention over the last several decades, as they offer a nature-friendly way to convert heat to electricity and to use electricity for refrigeration. Low-dimensional systems have come up as a viable option [22–25]. Monolayer TMDs are predicted to be excellent thermoelectric materials because of their relatively high effective mass and their property of valley degeneracy [26,27]. The Seebeck coefficient, which is one of the key parameters that decides the figure of merit of a thermoelectric material, has been found experimentally to be as high as 30 $mV\,K^{-1}$ in strictly monolayer MoS_2 (1L-MoS_2) [26], which is much more than that of any other nanoscale material [24,25]. Yet, it should be mentioned that only a handful of experimental studies have been carried out on the thermoelectrical properties of 1L-TMDs [26–28]. It will be interesting to explore how

*swarupdeb2580@phy.iitb.ac.in
†dhar@phy.iitb.ac.in

 © 2020 American Physical Society

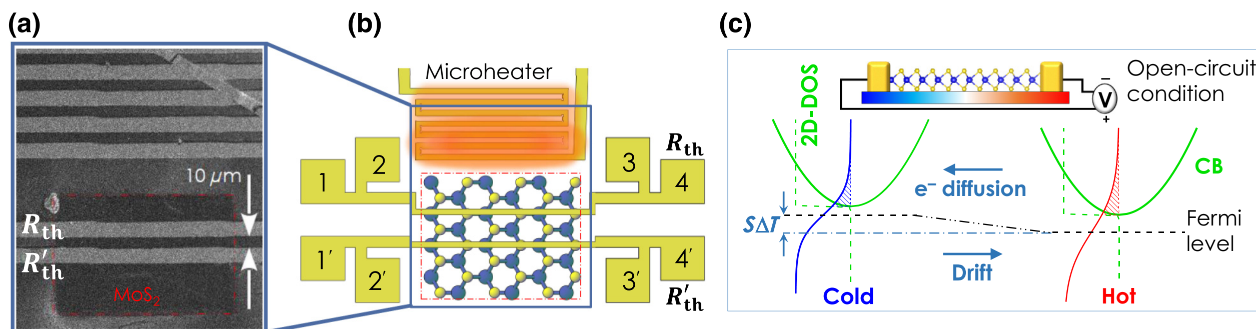

FIG. 1. (a) Scanning electron micrograph of an actual device. (b) Schematic illustration of the full device (not to scale). R_{th} (R'_{th}) is the four-probe resistance of the metal line that connects contact pads 1 and 2 (1′ and 2′) with pads 3 and 4 (3′ and 4′). The heater dimensions in the actual device are kept much larger than the length of the MoS_2 region to ensure temperature uniformity across the cross section. (c) Schematic illustration of the basic mechanism of charge flow and potential buildup across a semiconductor in the presence of a thermal gradient in an open-circuit configuration. The plus and minus signs indicate the polarity of the voltmeter probes. In the configuration shown, the measured thermoelectric voltage for an *n*-type semiconductor is negative.

surface adsorption affects the Seebeck coefficient of these materials.

Recently, we have developed a microcavity-based CVD growth technique, where 1L-MoS_2 films can be grown on *c*-sapphire substrates covering an area as large as a few square millimeters [29,30]. These films show a resistance of several gigaohms under ambient conditions [31]. Here, we study the thermoelectrical properties of these films under different environmental conditions before and after annealing in vacuum. A device, shown in Fig. 1(a), is fabricated on a continuous film using a photolithography technique. It is found that vacuum annealing at a temperature of about 525 K can reduce the resistance of the device by about six orders of magnitude, and at the same time the thermoelectric power is also reduced by almost an order of magnitude. Interestingly, both the resistance (R) and the Seebeck coefficient (S) return to their previous values when the sample is exposed to an oxygen environment. It is observed that the values of R and S for the device change significantly upon annealing. These values then hardly change as long as the device is not exposed to an oxygen environment. Our study attributes this effect to the passivation of sulfur-vacancy donors by oxygen molecules, which are physisorbed on the surface. Band-structure calculations within the framework of density-functional theory are performed to check the validity of the model. The theory shows that the adsorption of oxygen molecules at sulfur-vacancy sites is indeed energetically stable. This results in the formation of energy levels 250 meV below the donor states arising from the sulfur vacancies. It is also shown that these levels can capture electrons, which leads to the passivation of the donors.

II. EXPERIMENTAL METHODS

Strictly monolayer MoS_2 films are grown on *c*-sapphire substrates using a microcavity-based CVD technique. Prior to the growth, the substrates are cleaned successively in trichloroethylene, acetone, and methanol and finally dipped in a H_2O:HF (10:1) solution for 40 s. More details of the growth procedure have been discussed elsewhere [29,30]. A standard optical lithographic technique is used for device fabrication. Layers of two different metals, *viz.* titanium (approximately 20 nm) and gold (approximately 100 nm), are thermally deposited in a thermal evaporator in a background pressure less than 1×10^{-7} mbar. The device is subjected to rapid thermal annealing at a temperature of 300 °C for 1 min. Unwanted areas, which create an electrical contact between the microheater and the active area, are then selectively etched by dry oxygen plasma ashing. The positive photoresist S1813 is lithographically patterned to act as an etch mask for the dry etching. Figure 1(a) shows a scanning electron microscope image of part of the device in the vicinity of the microheater. Figure 1(b) shows a schematic depiction of the device. Pads 1 and 4 (1′ and 4′) are used as current probes, while pads 2 and 3 (2′ and 3′) are used as voltage probes for four-probe measurements of the resistivity of the two metal lines, which serve as resistive thermometers at the two locations. Contact pads 1 and 1′ are also used to perform two-probe measurements of current (I) versus voltage (V). I-V profiles are recorded using a Keithley 6487 picometer–voltage source. Two lock-in amplifiers (Signal Recovery 7225 and Stanford Research SR830, phase-locked with each other) are used to measure the four-probe resistances (R_{th} and R'_{th}) of the thermometers. A storage-type liquid-nitrogen cryostat is used to perform electrical and thermoelectric measurements at different temperatures ranging from 80 to 420 K. The chamber is also utilized for *in situ* annealing of the device in vacuum. Resistance (R)-versus-temperature (T) calibration of both of the microthermometers is carried out by slowly increasing the cryostat temperature from 80 to 420 K. A ramp rate of approximately 1 K min^{-1} is used during calibration to avoid a temperature lag between the

sensor (Pt-100) located in the cold finger and the device. After the calibration, one of the lock-in amplifiers (Signal Recovery 7225) is reconfigured to measure the temperature difference between the microthermometers in the device. Special care is taken to minimize the common-mode gain across the on-chip thermometers. A Keithley 6221 current source is used to excite the microheater. The thermoelectric voltage across the device is picked up using a Keithley 2182a nanovoltmeter, across terminals 1 and $1'$.

III. RESULTS AND DISCUSSION

Room-temperature I-V profiles for the device are shown in Fig. 2(a). The black symbols represent the data recorded before the sample space of the cryostat is evacuated. The resistance is measured to be approximately 26 GΩ. The profile represented by the red symbols is obtained after evacuating the sample space to approximately 1×10^{-5} mbar. Clearly, evacuation at room temperature has no significant effect on the resistance of the device. Also, note that the I-V profiles are quite linear for this highly resistive state. Next, the sample is heated using a cartridge heater embedded in the sample holder of the cryostat. Figure 2(b) shows a set of resistance-versus-temperature data recorded during successive steps of annealing of the sample.Evidently, in every step, R decreases with increasing T, which is expected for semiconductors. However, interestingly, R does not go back to the same value when the temperature is reduced to room temperature after each step of annealing. Rather, it follows a lower path to reach a smaller value. For example, the room-temperature resistance of the device before any annealing process is initiated is recorded to be approximately 230 MΩ. After the first and second annealing steps, R decreases to 128 and 44 MΩ, respectively. During the fourth annealing step, once the sample temperature has reached 420 K, the highest value achievable using the embedded heater, the microheater fabricated on the chip is switched on. The current through the microheater is increased to 75 mA in steps of 1 mA . These data are marked "4th." It is found that the microheater can raise the device temperature to 525 K. Interestingly, the resistance of the device shows a reduction by several orders of magnitude after this high-temperature annealing. An R-vs-T profile recorded during the fifth annealing step is also shown in Fig. 2(b). Clearly, in this step the rate of reduction of R with increasing T is much less than what is found in all the previous annealing steps. A room-temperature I-V profile for this lowest resistive state is also plotted in Fig. 2(a). In this state, the resistance is measured to be 32.8 kΩ, which is about six orders of magnitude less than the resistance measured before the sample goes through any annealing treatment. It is further noticed that the resistance is practically unchanged even after weeks in vacuum. These findings provide an opportunity to arrest the resistive state of the device at any desired value.

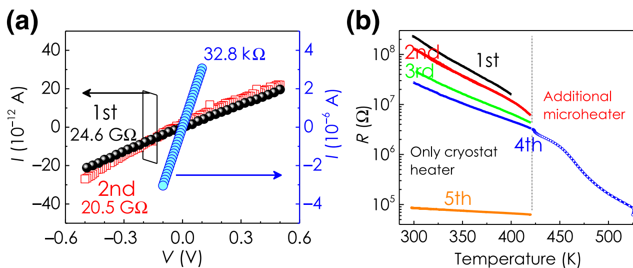

FIG. 2. (a) Current-voltage characteristics recorded at room temperature for the sample in different resistive states. (b) Plots of resistance (R) versus temperature recorded after different annealing steps. The numbers beside the profiles represent the sequence number of the annealing step. Temperature variation up to the vertical dotted line is achieved by an external heater, while the on-chip microheater is used additionally to reach higher temperature values.

Changes in the resistance after annealing can occur due to a variation in either carrier concentration or mobility, or in both. In order to track the changes of these parameters, we perform thermoelectric measurements at room temperature after taking the device to different resistive states. We start with a measurement of the Seebeck coefficient (S) of the sample when it is in the lowest-resistance state. Later, the sample space is successively purged with air to take the resistance to a higher value. Once a desired resistive state is achieved, the chamber is evacuated to approximately 1×10^{-5} mbar before carrying out the thermoelectric measurement. S is found to be negative in all cases, which suggests that electrons are the majority carriers in this system (i.e., it is n-type). The magnitude of S as a function of the resistance is plotted in Fig. 3(a). Clearly, $|S|$ increases with R.

The current under the influence of a temperature gradient in a semiconductor can be expressed as $I = G\,\Delta V + G_S\,\Delta T$ [32], where G is the conductance of the sample, and ΔT and ΔV are the temperature and potential difference, respectively, between the contacts. In an open-circuit configuration, since $I = 0$, the above equation leads to $\Delta V = -(G_s/G)\,\Delta T = S\,\Delta T$. The Seebeck coefficient S can thus be defined as the ratio between the diffusion current ($G_S\,\Delta T$) and the product of the conductance G and ΔT. While the diffusion current depends upon the difference between the carrier densities (δn) at the hot and cold ends of the device, the conductance G is proportional to the average carrier concentration n. Therefore, it can be said that the Seebeck coefficient is somewhat proportional to the ratio of these two quantities (δn and n) divided by ΔT, i.e., $S \sim \delta n/(n\,\Delta T)$. In an open-circuit configuration, the diffused charges accumulate on the colder end, which results in an upward shift of the Fermi level with respect to that of the warmer end. However, such a redistribution of carriers also leads to a potential difference between the two ends (the cooler end becomes higher in potential

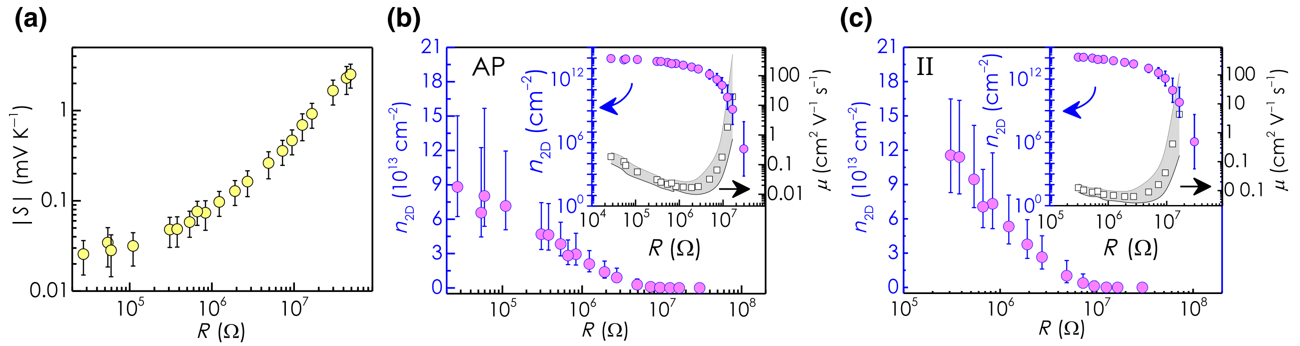

FIG. 3. (a) Magnitude of Seebeck coefficient ($|S|$) as a function of device resistance (R). (b),(c) Electron concentration (n_{2D}) obtained from S as a function of R after solving Eq. (1) for η with (b) $r = 0$ [acoustic-phonon (AP) scattering] and (c) $r = 1.5$ [ionized-impurity (II) scattering]. The insets show the variation of n_{2D} and the mobility (μ) on log-log plots.

for the electrons compared with the hotter end). A steady state is finally achieved when this built-in potential prevents any further diffusion from taking place. This situation is schematically depicted in Fig. 1(c). The ratio $\delta n/n$ is expected to decrease as the background carrier concentration n in the layer increases. As a result, $|S|$ decreases with increasing carrier density n. An analytical expression for S can be obtained by solving the linearized Boltzmann equation for G_s and G [33], which for 2D semiconductors takes the form [27]

$$S = -\frac{k_B}{q_e}\left[\eta - \frac{(2+r)\int_0^\infty f^{\,o}\epsilon^{r+1}\,d\epsilon}{(1+r)\int_0^\infty f^{\,o}\epsilon^{r}\,d\epsilon}\right], \quad (1)$$

where k_B is the Boltzmann constant, q_e is the electron charge, and $f^o = 1/[1+\exp(\epsilon-\eta)]$ is the Fermi distribution function. r is called the scattering exponent, and depends upon the type of scattering mechanism that limits the carrier relaxation time. In MoS_2, both acoustic phonons [27] and ionized-impurity or defect centers [34,35] have been shown to play a significant role in the scattering of electrons at room temperature. Note that for acoustic-phonon scattering, $r = 0$ [27], and for ionized-impurity scattering, $r = 1.5$ [36] in two dimensions. Equation (1) is solved to obtain $\eta = (E_f - E_c)/k_BT$ for $r = 0$ and 1.5 separately. Subsequently, the 2D electron concentration n_{2D} is estimated from $n_{2D} = 8\pi m^* k_B T h^{-2}\ln(1+e^\eta)$, where m^* and h represent the electronic effective mass and Planck's constant, respectively. The sheet carrier density n_{2D} extracted from S is plotted as a function of the measured resistance R of the device in Fig. 3(b) (for $r = 0$) and Fig. 3(c) (for $r = 1.5$). As expected, the carrier concentration in the sample decreases with increasing resistance. For a given resistance, the evaluated $n_{2D}|_{r=0}$ turns out to be less than $n_{2D}|_{r=1.5}$ by a small factor. However, the qualitative nature of the variation of n_{2D} with R remains the same in both cases. A lower-bound estimate of the mobility μ can be made from n_{2D} and R through $\mu = l/(bRn_{2D}q_e)$, where l and b are the length and width, respectively, of the device. The insets in Fig. 3(b) (for $r = 0$) and Fig. 3(c) (for $r = 1.5$) portray both μ and n_{2D} as functions of R on a logarithmic scale. It is interesting to note that beyond a threshold value of R, both of these parameters show a sharp change: n_{2D} decreases by several orders of magnitude, and at the same time μ increases significantly.

All these observations point towards the fact that the environment surrounding these 1L-MoS_2 films plays an important role in governing their resistance. For better understanding, we measure the resistance of the device in different controlled environments. The results are shown in Fig. 4. The sample is first annealed and taken to a state where the resistance is approximately 50 kΩ. The sample space is then flushed with argon (Ar) gas (99.999% pure, oxygen ≤2 ppm, moisture ≤2 ppm). Clearly, there is no significant increment in the device resistance as a result of the Ar exposure. About an hour later, the sample space is evacuated. The same procedure is repeated with nitrogen

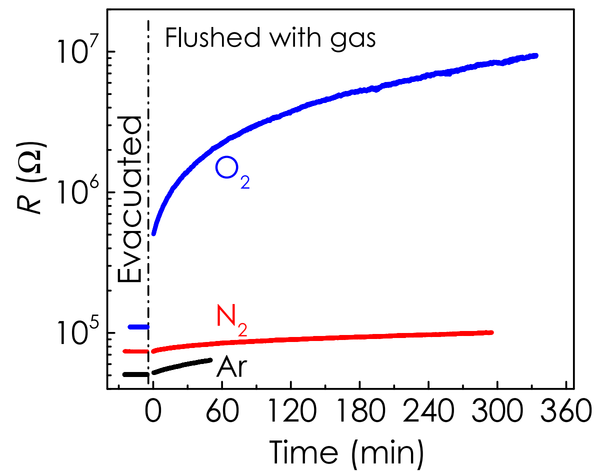

FIG. 4. Change in resistance of the device after the sample is exposed to different environments. The conductivity of the channel is reduced drastically after introduction of O_2 into the sample space.

(N_2) (99.999% pure, oxygen ≤ 2 ppm, moisture ≤ 2 ppm). In this case as well, the change in resistance is not significant, which is obvious from the fact that even after approximately 5 h of exposure, the resistance increases by a factor of only 1.3. However, the resistance changes dramatically when oxygen (99.999% pure, nitrogen $\leq$ 5 ppm, moisture ≤ 2 ppm) is finally introduced into the chamber. Within a few minutes, R is increased by an order of magnitude, and after 5.5 h, R is enhanced by about two orders of magnitude.

A. Theory

The observations in Figs. 3 and 4 clearly suggest that adsorption and desorption of oxygen molecules at the surface must be the reason for the dramatic change in the carrier density in the layer. It should be noted that sulfur vacancies have been shown to be the most abundant type of point defect in MoS_2, especially in CVD-grown MoS_2. Among the different types of sulfur vacancy that can exist in a monolayer film, same-side disulfur vacancies, SV_2 (the absence of two sulfur ions from the same side of a unit cell), are expected to act as donors [15,16]. We believe that under ambient conditions, adsorption of oxygen molecules at these vacancy sites passivates the donors, resulting in a reduction of the electron concentration in the conduction band. Upon vacuum annealing, these molecules are removed from the surface and the electron concentration recovers. The range of temperature involved in these experiments, as well as the reversible nature of the phenomenon, suggests that the oxygen molecules must be physisorbed (not chemisorbed) on the surface.

In order to check the feasibility of this hypothesis, theoretical calculations are carried out within the framework of density-functional theory [37] by employing the Vienna *ab initio* simulation package (VASP) [38,39]. For this purpose, we use projector-augmented-wave pseudopotentials [38,40] with a kinetic-energy cutoff of 450 eV, and the Perdew-Burke-Ernzerhof exchange-correlation functional [41]. To optimize the structures, we employ a k-mesh of size $5 \times 5 \times 1$, while for density-of-states calculations, a $21 \times 21 \times 1$ k-grid is used. The total-energy and force convergence criteria are chosen to be 10^{-6} eV and $0.02\,\text{eV}\,\text{Å}^{-1}$, respectively. The effects of spin polarization and spin-orbit coupling are also included in our calculations. In this work, the van der Waals force correction is incorporated using the DFT-D3 method [42]. For the relaxed structure, the pressure in the supercell is less than 0.2 kbar. At least 20 Å of vacuum is introduced along the c direction to minimize spurious interactions. To perform the band-structure calculations, 60 k-points are considered in reciprocal space. A 4×4 supercell is considered to understand the nature of the interaction of O_2 molecules with sulfur vacancies in the MoS_2 monolayer. Two sulfur atoms are removed from same side of the unit cell, as shown in Fig. 5(a).

The calculations show that the vacancy SV_2 acts as a donor state and gives rise to several new energy states in the forbidden gap, as presented in Fig. 5(b) (colored blue in the figure). Note that the top of the donor band lies approximately 0.25 eV below the conduction-band minimum. These donor states appear due to the hybridization of weak sulfur $3p$ and strong molybdenum $4d$ orbitals. It should be noted that this finding is in good agreement with theoretical predictions made earlier [43].

In order to look into the effect of O_2 adsorption at the surface, we first carry out geometry relaxation with the O_2 molecule placed at an initial-guess position. The energetically most favorable site for attachment turns out to be on top of either of the vacancy sites in the defect and approximately 0.19 nm above the monolayer surface. Top and side views of the complex system (1L-MoS_2 with $SV_2 + O_2$) are depicted in Fig. 5(c). In Fig. 5(d), the band structure calculated for the $SV_2 + O_2$ complex is shown. The attachment of O_2 creates two flat bands (red lines) that are approximately 250 meV below the donor levels. The rest of the band structure remains almost the same as that obtained for 1L-MoS_2 with SV_2. The difference in charge density due to O_2 adsorption can be described as $\rho_{\text{ad}} = \rho_{\text{MoS}_2+SV_2+\text{O}_2} - \rho_{\text{MoS}_2+SV_2} - \rho_{O_2}$, where $\rho_{\text{MoS}_2+SV_2+O_2}$, $\rho_{\text{MoS}_2+SV_2}$, and ρ_{O_2} are the charge densities of 1L-MoS_2 with SV_2 plus adsorbed O_2, 1L-MoS_2 with SV_2, and an isolated O_2 molecule, respectively. A differential charge-density plot for the complex system is presented in Fig. 5(e). Note that upon adsorption of an O_2 molecule, the 1L-MoS_2 loses electrons, while these are accumulated around the O_2 molecule, suggesting electron transfer from the SV_2 defects to O_2 molecules, which is also consistent with the appearance of energy levels (red lines) below the SV_2 donor states when O_2 is adsorbed at the SV_2 defect site, as shown in Fig. 5(d). The theory thus supports the picture that the adsorption of O_2 molecules passivates SV_2 donor states by introducing a lower-energy state that traps these electrons. The formation energy of the $SV_2 + O_2$ complex is estimated to be approximately 340 meV, suggesting weak bonding of the O_2 molecules to the surface. This the reason why O_2 molecules are efficiently detached from the surface at elevated temperatures and in high vacuum, which results in a drastic increase in the conductivity as observed experimentally.

Here, we show that the transport and thermoelectrical properties of 1L-MoS_2 can be controlled by adopting an appropriate thermal-annealing and oxygen-exposure recipe. However, when the system is taken out of the vacuum, the adsorption of ambient oxygen destroys the state achieved. One must find an encapsulating material that can arrest the conducting state even under ambient conditions to ensure reliable operation of 1L-MoS_2-based transistors. On the other hand, one can also exploit the significant role of oxygen adsorption in the resistive properties of 1L-MoS_2 to use such films in oxygen-sensing applications. It

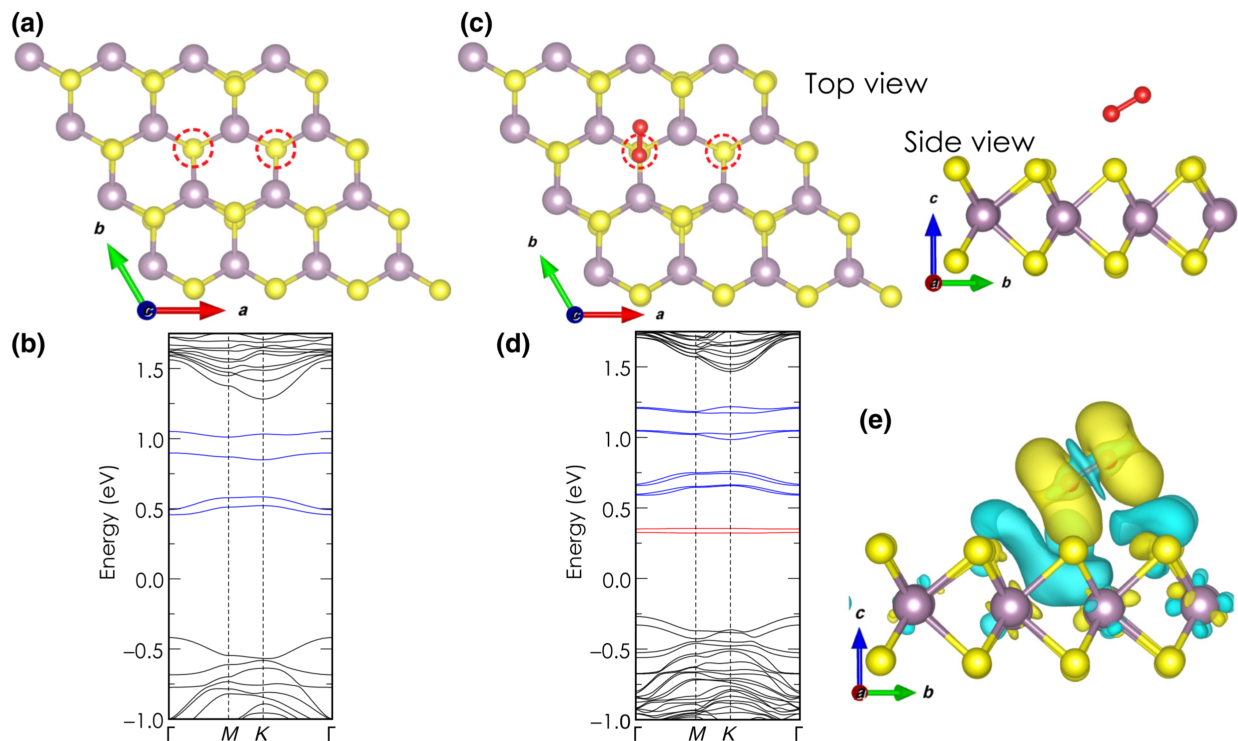

FIG. 5. (a) Relaxed geometry (4 × 4 supercell) and (b) band structure of a MoS_2 monolayer with SV_2. The bands colored blue appear due to the inclusion of a vacancy in the structure. (c) Relaxed geometry and (d) band structure of the complex system (O_2 adsorbed on MoS_2 monolayer with SV_2). The bands colored red in the gap region are predominantly contributed by the O_2 molecule. (e) Side view of a differential charge-density plot of the complex system with an isovalue of 9.8×10^{-5} e Å^{-3}, where a yellow color indicates an electron-rich region and a cyan color denotes the loss of electrons.

should be noted that there have been a large number of theoretical and experimental studies on the prospects of MoS_2 for use in various gas-sensing applications [44–50]. Tong *et al.* [48] have experimentally studied the effect of oxygen adsorption on the resistance of four-layer MoS_2. They reported a qualitatively similar trend of a resistance change due to oxygen adsorption.

IV. CONCLUSIONS

In conclusion, adsorption of oxygen molecules at sulfur-vacancy sites in 1L-MoS_2 layers results in the formation of electron traps, which lie 250 meV below the donor levels introduced by these vacancies. As a result, these donors are passivated, and an as-grown layer that is exposed to ambient conditions becomes highly resistive. It is found that the resistance and thermoelectric power of the material can be varied to a large extent through annealing. Once established, these parameters remain unchanged unless the layer is exposed to an oxygen environment. Annealing followed by an effective encapsulation method may offer a unique way to control doping in the material, which is an important milestone towards technological applications.

ACKNOWLEDGMENTS

We acknowledge financial support by the Council of Scientific & Industrial Research of the Government of India under Grant No. 03(1403)/17/EMR II. We thank the Centre of Excellence in Nanoelectronics (CEN) at IIT Bombay for providing various experimental facilities.

[1] Kallol Roy, Tanweer Ahmed, Harshit Dubey, T. Phanindra Sai, Ranjit Kashid, Shruti Maliakal, Kimberly Hsieh, Saquib Shamim, and Arindam Ghosh, Number-resolved single-photon detection with ultralow noise van der Waals hybrid, Adv. Mater. **30**, 1704412 (2018).

[2] Dmitrii Unuchek, Alberto Ciarrocchi, Ahmet Avsar, Zhe Sun, Kenji Watanabe, Takashi Taniguchi, and Andras Kis, Valley-polarized exciton currents in a van der Waals heterostructure, Nat. Nanotechnol. **14**, 1104 (2019).

[3] Kirby K. H. Smithe, Chris D. English, Saurabh V. Suryavanshi, and Eric Pop, High-field transport and velocity saturation in synthetic monolayer MoS_2, Nano Lett. **18**, 4516 (2018).

[4] David J. Hynek, Joshua V. Pondick, and Judy J. Cha, The development of 2D materials for electrochemical energy applications: A mechanistic approach, APL Mater. **7**, 030902 (2019).

[5] Yanhao Tang, Kin Fai Mak, and Jie Shan, Long valley lifetime of dark excitons in single-layer WSe_2, Nat. Commun. **10** (2019).

[6] Joshua V. Pondick, John M. Woods, Jie Xing, Yu Zhou, and Judy J. Cha, Stepwise sulfurization from MoO_3 to MoS_2 via chemical vapor deposition, ACS Appl. Nano Mater. **1**, 5655 (2018).

[7] D. Dumcenco, D. Ovchinnikov, O. L. Sanchez, P. Gillet, D. T. L. Alexander, S. Lazar, A. Radenovic, and A. Kis, Large-area MoS_2 grown using H_2S as the sulphur source, 2D Mater. **2**, 044005 (2015).

[8] P. Budania, P. T. Baine, J. H. Montgomery, D. W. McNeill, S. J. N. Mitchell, M. Modreanu, and P. K. Hurley, Effect of post-exfoliation treatments on mechanically exfoliated MoS_2, Mater. Res. Express **4**, 025022 (2017).

[9] Gábor Zsolt Magda, János Petö, Gergely Dobrik, Chanyong Hwang, László P. Biró, and Levente Tapasztó, Exfoliation of large-area transition metal chalcogenide single layers, Sci. Rep. **5**, 14714 (2015).

[10] S. H. Baek, Y. Choi, and W. Choi, Large-area growth of uniform single-layer MoS_2 thin films by chemical vapor deposition, Nanoscale Res. Lett. **10**, 388 (2015).

[11] Kirby K. H. Smithe, Saurabh V. Suryavanshi, Miguel Muñoz Rojo, Aria D. Tedjarati, and Eric Pop, Low variability in synthetic monolayer MoS_2 devices, ACS Nano **11**, 8456 (2017).

[12] Dumitru Dumcenco, Dmitry Ovchinnikov, Kolyo Marinov, Predrag Lazi, Marco Gibertini, Nicola Marzari, Oriol Lopez Sanchez, Yen-Cheng Kung, Daria Krasnozhon, Ming-Wei Chen, Simone Bertolazzi, Philippe Gillet, Anna Fontcuberta i Morral, Aleksandra Radenovic, and Andras Kis, Large-area epitaxial monolayer MoS_2, ACS Nano **9**, 4611 (2015).

[13] Sina Najmaei, Matin Amani, Matthew L. Chin, Zheng Liu, A. Glen Birdwell, Terrance P. O'Regan, Pulickel M. Ajayan, Madan Dubey, and Jun Lou, Electrical transport properties of polycrystalline monolayer molybdenum disulfide, ACS Nano **8**, 7930 (2014).

[14] Oleg V. Yazyev and Yong P. Chen, Polycrystalline graphene and other two-dimensional materials, Nat. Nanotechnol. **9**, 755 (2014).

[15] Vinod K. Sangwan, Deep Jariwala, In Soo Kim, Kan-Sheng Chen, Tobin J. Marks, Lincoln J. Landhon, and Mark C. Hersam, Gate-tunable memristive phenomena mediated by grain boundaries in single-layer MoS_2, Nat. Nanotechnol. **10**, 403 (2015).

[16] Vinod K. Sangwan, Hong-Sub Lee, Hadallia Bergeron, Itamar Balla, Megan E. Beck, Kan-Sheng Chen, and Mark C. Hersam, Multi-terminal memtransistors from polycrystalline monolayer molybdenum disulfide, Nature **554**, 500 (2018).

[17] Sefaattin Tongay, Joonki Suh, Can Ataca, Wen Fan, Alexander Luce, Jeong Seuk Kang, Jonathan Liu, Changhyun Ko, Rajamani Raghunathanan, Jian Zhou, Frank Ogletree, Jingbo Li, Jeffrey C. Grossman, and Junqiao Wu, Defects activated photoluminescence in two-dimensional semiconductors: Interplay between bound, charged and free excitons, Sci. Rep. **3**, 2657 (2013).

[18] Rahul Rao, Victor Carozo, Yuanxi Wang, Ahmad E. Islam, Nestor Perea-Lopez, Kazunori Fujisawa, Vincent H. Crespi, Mauricio Terrones, and Benji Maruyama, Dynamics of cleaning, passivating and doping monolayer MoS_2 by controlled laser irradiation, 2D Mater. **6**, 045031 (2019).

[19] Kwanghee Park, Haneul Kang, Seonghyun Koo, DaeEung Lee, and Sunmin Ryu, Redox-governed charge doping dictated by interfacial diffusion in two-dimensional materials, Nat. Commun. **10**, 4931 (2019).

[20] Pranjal Kumar Gogoi, Zhenliang Hu, Qixing Wang, Alexandra Carvalho, Daniel Schmidt, Xinmao Yin, Yung-Huang Chang, Lain-Jong Li, Chorng Haur Sow, A. H. Castro Neto, Mark B. H. Breese, Andrivo Rusydi, and Andrew T. S. Wee, Oxygen Passivation Mediated Tunability of Trion and Excitons in MoS_2, Phys. Rev. Lett. **119**, 077402 (2017).

[21] Sefaattin Tongay, Jian Zhou, Can Ataca, Jonathan Liu, Jeong Seuk Kang, Tyler S. Matthews, Long You, Jingbo Li, Jeffrey C. Grossman, and Junqiao Wu, Broad-range modulation of light emission in two-dimensional semiconductors by molecular physisorption gating, Nano Lett. **13**, 2831 (2013).

[22] Srijit Goswami, Christoph Siegert, Matthias Baenninger, Michael Pepper, Ian Farrer, David A. Ritchie, and Arindam Ghosh, Highly Enhanced Thermopower in Two-Dimensional Electron Systems at Millikelvin Temperatures, Phys. Rev. Lett. **103**, 026602 (2009).

[23] Chul-Ho Lee, Gyu-Chul Yi, Yuri M. Zuev, and Philip Kim, Thermoelectric power measurements of wide band gap semiconducting nanowires, Appl. Phys. Lett. **94**, 022106 (2009).

[24] Peng Wei, Wenzhong Bao, Yong Pu, Chun Ning Lau, and Jing Shi, Anomalous Thermoelectric Transport of Dirac Particles in Graphene, Phys. Rev. Lett. **102**, 166808 (2009).

[25] Stefano Roddaro, Daniele Ercolani, Mian Akif Safeen, Soile Suomalainen, Francesco Rossella, Francesco Giazotto, Lucia Sorba, and Fabio Beltram, Giant thermovoltage in single inas nanowire field-effect transistors, Nano Lett. **13**, 3638 (2013).

[26] Jing Wu, Hennrik Schmidt, Kiran Kumar Amara, Xiangfan Xu, Goki Eda, and Barbaros Zyilmaz, Large thermoelectricity via variable range hopping in chemical vapor deposition grown single-layer MoS_2, Nano Lett. **14**, 2730 (2014).

[27] Kedar Hippalgaonkar, Ying Wang, Yu Ye, Diana Y. Qiu, Hanyu Zhu, Yuan Wang, Joel Moore, Steven G. Louie, and Xiang Zhang, High thermoelectric power factor in two-dimensional crystals of Mos_2, Phys. Rev. B **95**, 115407 (2017).

[28] Michele Buscema, Maria Barkelid, Val Zwiller, Herre S. J. van der Zant, Gary A. Steele, and Andres Castellanos-Gomez, Large and tunable photothermoelectric effect in single-layer MoS_2, Nano Lett. **13**, 358 (2013).

[29] P. K. Mohapatra, S. Deb, B. P. Singh, P. Vasa, and S. Dhar, Strictly monolayer large continuous MoS_2 films on diverse substrates and their luminescence properties, Appl. Phys. Lett. **108**, 042101 (2016).

[30] Swarup Deb, Poulab Chakrabarti, Pranab K. Mohapatra, Barun K. Barick, and Subhabrata Dhar, Tailoring of defect luminescence in CVD grown monolayer MoS_2 film, Appl. Surf. Sci. **445**, 542 (2018).

[31] Swarup Deb, Poulab Chakrabarti, Himadri Chakraborti, Kantimay Das Gupta, and Subhabrata Dhar, Thermally

stimulated current spectroscopy of traps in CVD grown monolayer MoS_2, Appl. Phys. Lett. **115**, 032104 (2019).

[32] I. Terasaki, in *Materials for Energy Conversion Devices*, edited by Charles C. Sorrell, Sunao Sugihara, and Janusz Nowotny (Woodhead Publishing, 2005), p. 339. https://doi.org/10.1533/9781845690915.3.339

[33] Xinyue Zhang and Yanzhong Pei, Manipulation of charge transport in thermoelectrics, npj Quantum Mater. **2**, 68 (2017).

[34] Subhamoy Ghatak, Atindra Nath Pal, and Arindam Ghosh, Nature of electronic states in atomically thin MoS_2 field-effect transistors, ACS Nano **5**, 7707 (2011).

[35] Kristen Kaasbjerg, Tony Low, and Antti-Pekka Jauho, Electron and hole transport in disordered monolayer MoS_2: Atomic vacancy induced short-range and Coulomb disorder scattering, Phys. Rev. B **100**, 115409 (2019).

[36] John H. Davies, *The Physics of Low-Dimensional Semiconductors: An Introduction* (Cambridge University Press, Cambridge, 1998).

[37] W. Kohn and L. J. Sham, Self-consistent equations including exchange and correlation effects, Phys. Rev. **140**, A1133 (1965).

[38] G. Kresse and J. Furthmüller, Efficient iterative schemes for Ab initio total-energy calculations using a plane-wave basis set, Phys. Rev. B **54**, 11169 (1996).

[39] G. Kresse and J. Furthmüller, Efficiency of Ab-initio total energy calculations for metals and semiconductors using a plane-wave basis set, Comput. Mater. Sci. **6**, 15 (1996).

[40] P. E. Blöchl, Projector augmented-wave method, Phys. Rev. B **50**, 17953 (1994).

[41] John P. Perdew, Kieron Burke, and Matthias Ernzerhof, Generalized Gradient Approximation Made Simple, Phys. Rev. Lett. **77**, 3865 (1996).

[42] Stefan Grimme, Jens Antony, Stephan Ehrlich, and Helge Krieg, A consistent and accurate Ab initio parametrization of density functional dispersion correction (DFT-D) for the 94 elements h-pu, J. Chem. Phys. **132**, 154104 (2010).

[43] Hao Qiu, Tao Xu, Zilu Wang, Wei Ren, Haiyan Nan, Zhenhua Ni, Qian Chen, Shijun Yuan, Feng Miao, Fengqi Song, Gen Long, Yi Shi, Litao Sun, Jinlan Wang, and Xinran Wang, Hopping transport through defect-induced localized states in molybdenum disulphide, Nat. Commun. **4**, 2642 (2013).

[44] Hai Li, Zongyou Yin, Qiyuan He, Hong Li, Xiao Huang, Gang Lu, Derrick Wen Hui Fam, Alfred Iing Yoong Tok, Qing Zhang, and Hua Zhang, Fabrication of single-and multilayer MoS_2 film-based field-effect transistors for sensing no at room temperature, Small **8**, 63 (2012).

[45] Byungjin Cho, Ah Ra Kim, Youngjin Park, Jongwon Yoon, Young-Joo Lee, Sangchul Lee, Tae Jin Yoo, Chang Goo Kang, Byoung Hun Lee, Heung Cho Ko, *et al.*, Bifunctional sensing characteristics of chemical vapor deposition synthesized atomic-layered MoS_2, ACS Appl. Mater. Interfaces **7**, 2952 (2015).

[46] Byungjin Cho, Myung Gwan Hahm, Minseok Choi, Jongwon Yoon, Ah Ra Kim, Young-Joo Lee, Sung-Gyu Park, Jung-Dae Kwon, Chang Su Kim, Myungkwan Song, *et al.*, Charge-transfer-based gas sensing using atomic-layer MoS_2, Sci. Rep. **5**, 8052 (2015).

[47] Qiyuan He, Zhiyuan Zeng, Zongyou Yin, Hai Li, Shixin Wu, Xiao Huang, and Hua Zhang, Fabrication of flexible MoS_2 thin-film transistor arrays for practical gas-sensing applications, Small **8**, 2994 (2012).

[48] Yu Tong, Zhenhua Lin, John T. L. Thong, Daniel S. H. Chan, and Chunxiang Zhu, MoS_2 oxygen sensor with gate voltage stress induced performance enhancement, Appl. Phys. Lett. **107**, 123105 (2015).

[49] Yeon Hoo Kim, Kye Yeop Kim, You Rim Choi, Young-Seok Shim, Jong-Myeong Jeon, Jong-Heun Lee, Soo Young Kim, Seungwu Han, and Ho Won Jang, Ultrasensitive reversible oxygen sensing by using liquid-exfoliated MoS_2 nanoparticles, J. Mater. Chem. A **4**, 6070 (2016).

[50] Qu Yue, Zhengzheng Shao, Shengli Chang, and Jingbo Li, Adsorption of gas molecules on monolayer MoS_2 and effect of applied electric field, Nanoscale Res. Lett. **8**, 425 (2013).